Two-dimensional growth of dendritic islands of NTCDA on Cu(001) studied in real time – Supporting Information

Janina Felter,* Markus Franke,* Jana Wolters, Caroline Henneke, and Christian Kumpf
Peter Grünberg Institut (PGI-3), Forschungszentrum Jülich, 52425 Jülich, Germany and
Jülich Aachen Research Alliance (JARA)–Fundamentals of Future Information Technology, 52425 Jülich, Germany
(Dated: December 19, 2018)

I. LEEM AND LEED MEASUREMENTS DURING DEPOSITION

The growth of NTCDA on Cu(001) has been studied in the coverage regime up to 2.0 ML using LEEM and LEED in real time during the deposition process. In addition to the selected images shown in the main manuscript, we present full series of (bright-field) LEEM and LEED images here.

Figure 1 shows nine BF-LEEM images in the sub-monolayer regime. Beside step edges and point-like defects, no delimited details can be seen, only the overall intensity decreases with increasing coverage. This observation also holds for different focus settings (images not shown).

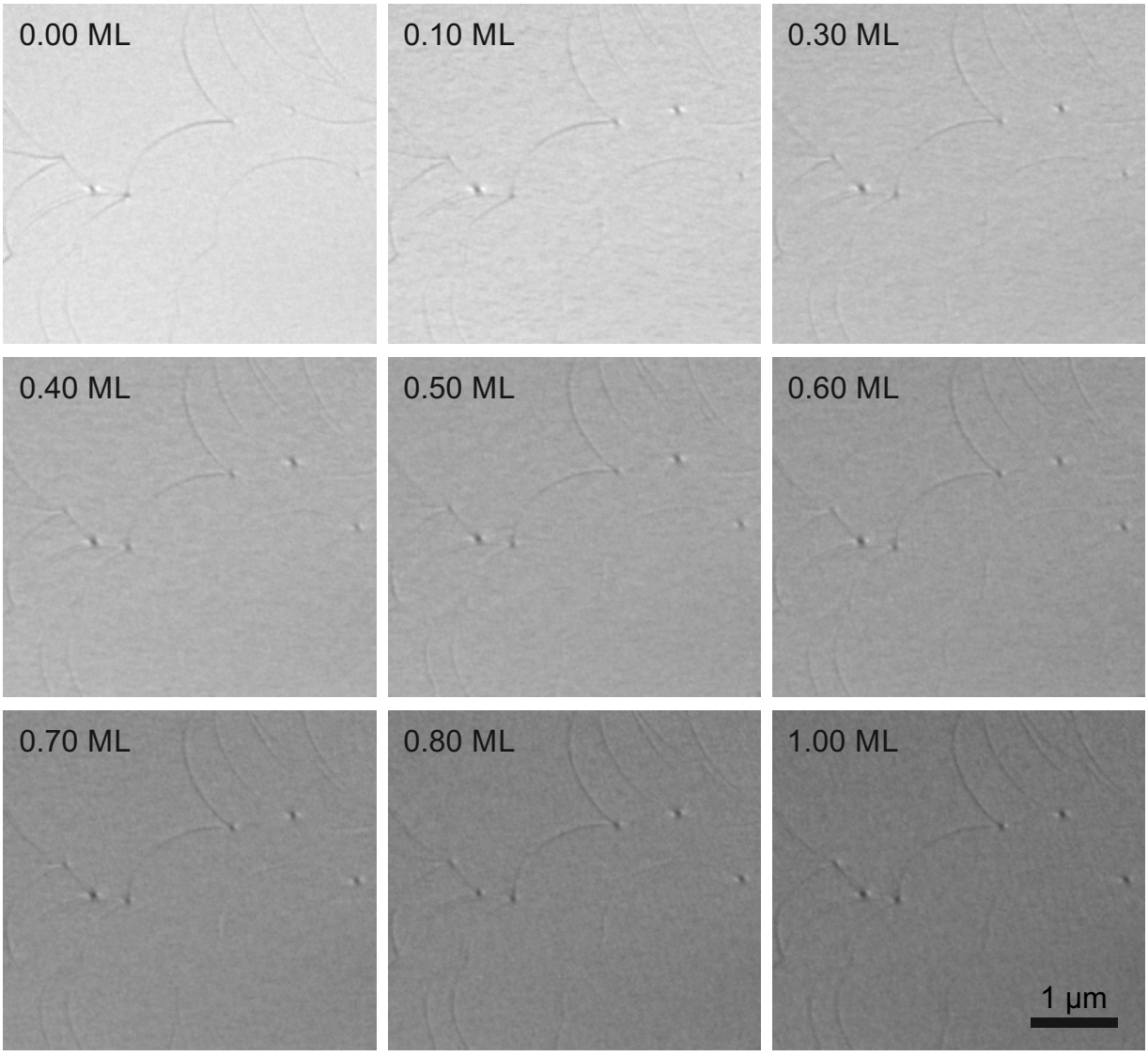

FIG. 1. BF-LEEM images taken during deposition of the first layer of NTCDA on Cu(001) ($U_{\mathrm{start}} = 2$ V).

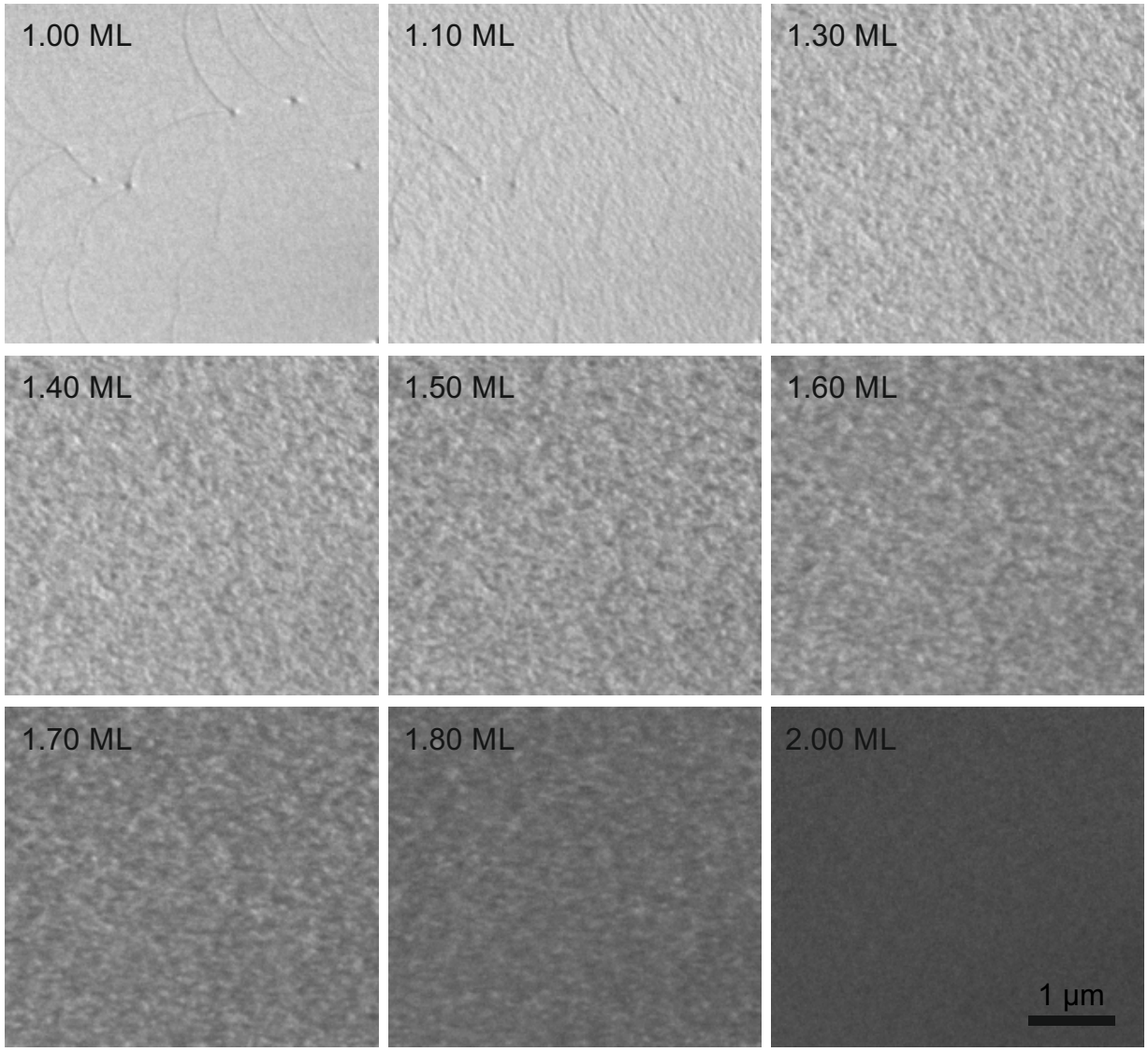

FIG. 2. BF-LEEM images taken during deposition of the second layer of NTCDA on Cu(001). The start voltage is unchanged compared to Fig. 1 ($U_{\mathrm{start}} = 2$ V), but the contrast of the images has been adjusted.

For coverages between 1 and 2 ML, the BF-LEEM images are shown in Fig. 2. The nucleation of the second layer can be seen in form of small dark islands growing larger and larger with increasing coverage. Hence, the second layer grows in form of small compact NTCDA islands.

Note that coverages could be determined with an uncertainty smaller than 0.03 ML in LEEM. This relatively high precision is due to the fact that the observed overall LEEM intensity reduces linearly with increasing coverage, which can be observed very well in LEEM. Since the deposition rate was very constant in our experiments, the main error in determining the coverages stems from the uncertainty to determine the time when the first monolayer is closing. This causes a small plateau in the intensity vs. time plot, as can be seen in Fig. 2(e) of the main manuscript after 56 min deposition time. An estimated error of 3% for this point in time results in a maximum uncertainty of 0.03 ML for the coverages determined via the deposition time in the LEEM instrument. For the STM and XSW experiments the uncertainties are larger ($0.05 - 0.1$ ML), since no measure for the linearity of the deposition rate is available.

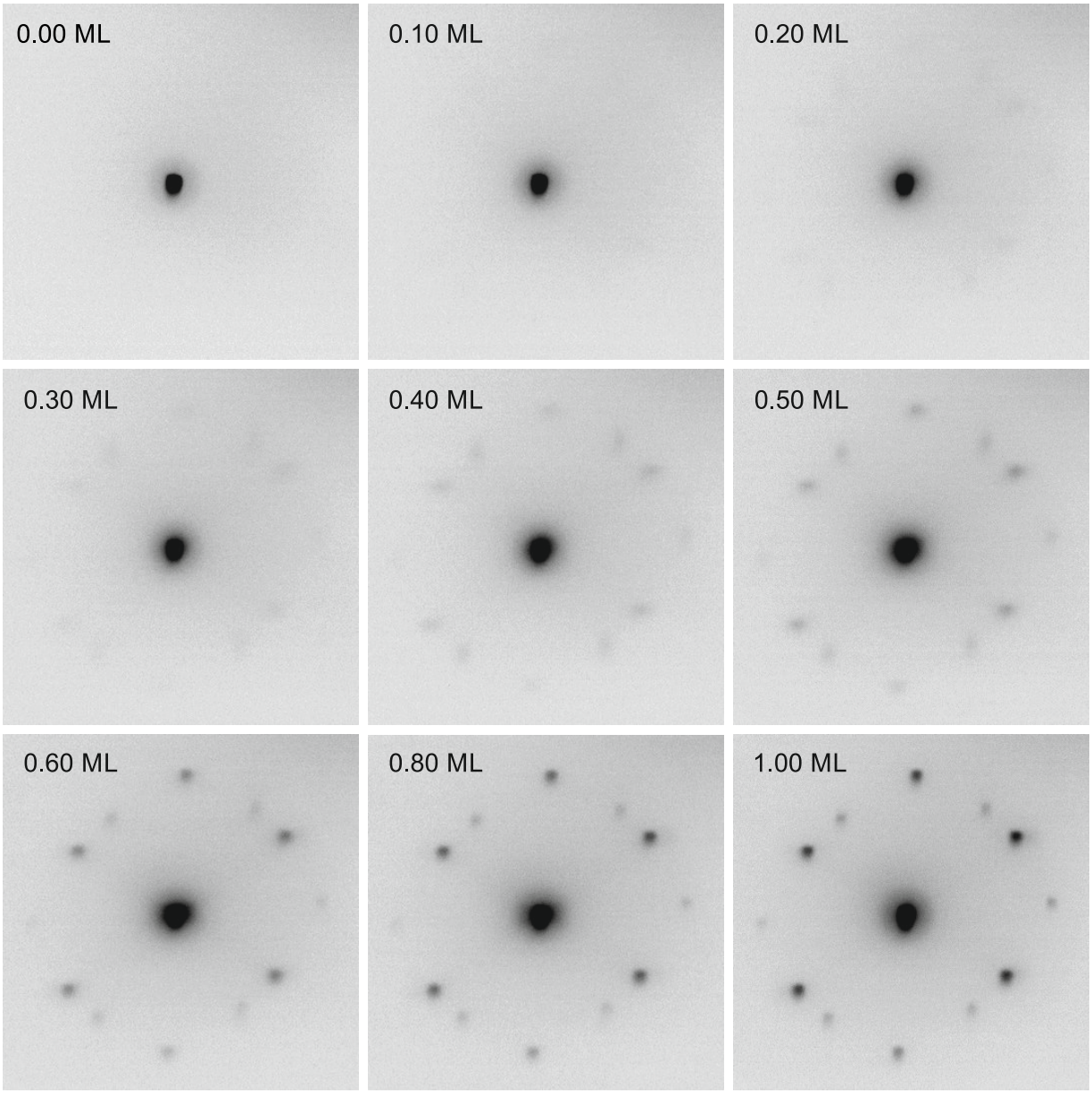

FIG. 3. LEED images taken during deposition of the first layer of NTCDA on Cu(001) ($U_{\mathrm{start}} = 7.5$ V).

In Fig. 3, we show LEED images taken during the deposition of the first layer of NTCDA on Cu(001). It can clearly be seen that a decent LEED pattern arises at ≈ 0.2 ML, and becomes sharper and more intense with rising coverage. While in the beginning the LEED spots are elongated, above ≈ 0.6 ML they become round indicating isotropic islands. The LEED pattern corresponds to the superstructure found by Fink et al. [1].

II. CHANGES DURING CONSECUTIVE STM SCANS

We have tested the stability of the NTCDA islands on Cu(001) by consecutive scanning of the same surface region for many times. In Fig. 4 (a-c), we depict a series of such STM images for a sample in the low submonolayer coverage regime. The molecular islands appear dark on a brighter copper surface. In the three consecutive images, we see only small changes in the island size and shape, as exemplarily indicated by red and blue ovals. As discussed in the main manuscript, the orientation of the unit cell of the NTCDA structure is clearly correlated to the preferred growth directions of the islands, leading to elongated island shapes. In panels (d-f), we indicate the two possible domain orientations of the islands by coloring them in red and blue, and we indicate the contour of the domains by a black line, comprising several identically oriented islands. In the three consecutive images, we find that these contour lines show only small changes due to repeatedly scanning this surface region. Hence, tip-induced or diffusion-related changes do occur to some extend, but they are not significantly changing the shape of both individual islands and domain areas.

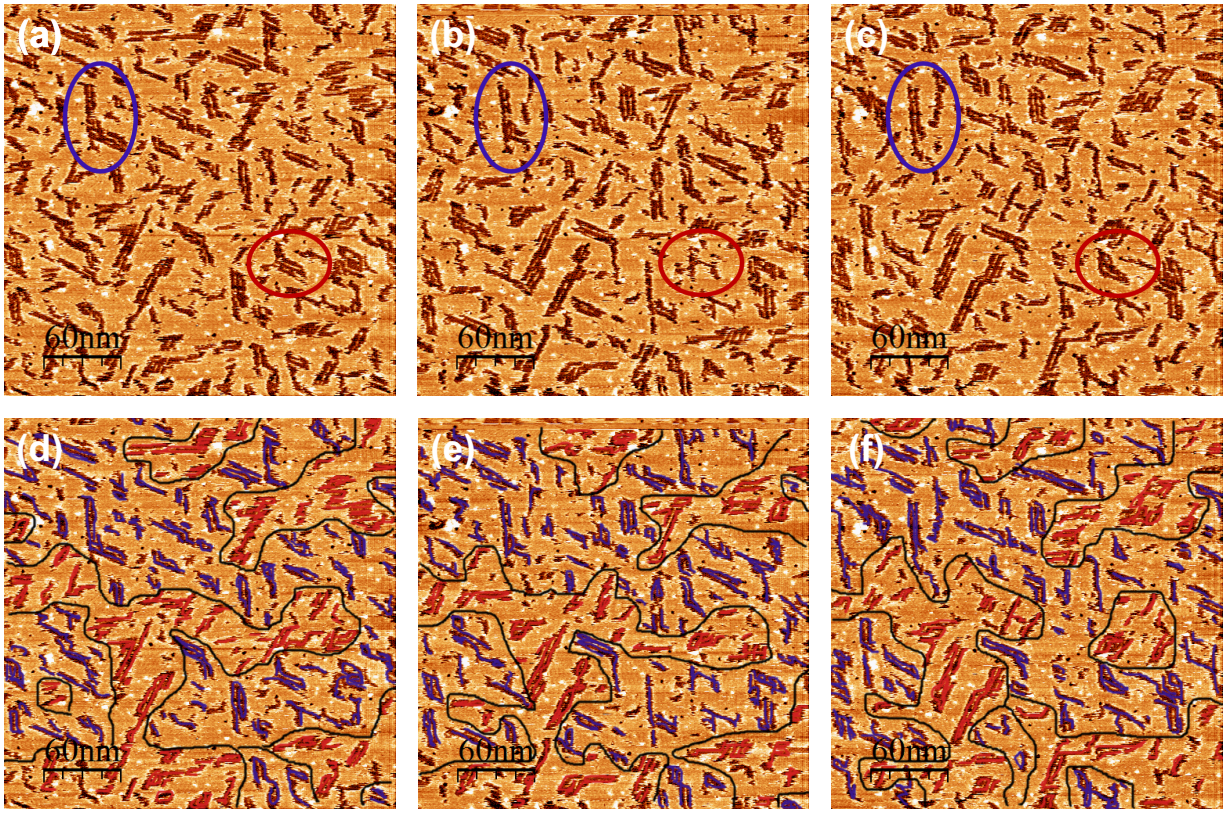

FIG. 4. (a-c) STM images of a low coverage sample of NTCDA on Cu(001) recorded consecutively on the same area on the sample. (d-f) The islands are color coded according to their domain orientation in red and blue, and black lines indicate the corresponding domain boundaries. $V_{\mathrm{gap}} = -0.75$ V, $I_{\mathrm{tunnel}} = 0.03$ nA.

III. Treatment of non-dipolar effects in normal incidence x-ray standing waves

In XSW, non-dipolar effects usually cannot be neglected since rather high photon energies have to be used in order to fulfill the Bragg condition of the selected bulk Bragg reflection. We have performed our NIXSW data analysis within the so-called "dipole+quadrupole" approximation (for details see Bocquet et al. [2]). Within this approximation, the XSW yield curve is described (and fitted) by the equation

$$Y = 1 + S_{\mathrm{R}}R + 2|S_{\mathrm{I}}|\sqrt{R}F^H\cos(\nu - 2\pi P^H + \psi), \tag{1}$$

see eq. 46 in Ref. [2] and eq. 13 in Ref. [3]. Beside the reflectivity R of the Bragg reflection, the fit parameters coherent fraction F^H and position P^H, and the phase of the standing wave field ν, this equation also contains the non-dipolar correction factors S_{R} and $S_{\mathrm{I}} = |S_{\mathrm{I}}| \cdot \exp(i\psi)$. Note that S_{R} and S_{I} depend on the angle ϕ between the incident synchrotron beam and the direction towards the analyzer, and also on the angle 2θ between the incident x-ray beam and the Bragg diffracted beam (with θ being the Bragg angle). While in perfect normal incidence geometry $2\theta = 180°$, in reality this value is never precisely realized since the intensity of the diffracted beam must be recorded by any kind of detector, which then would block the incident beam. Although the deviation from perfect normal incidence is usually small (in our case $\xi = 90° - \theta \approx 3.5°$), the effect is not negligible as demonstrated by van Straaten et al. recently [3].

Alternatively, non-dipolar effects can also be parameterized by γ and Δ, which quantify the contribution of the emitted d-wave to the photoemission intensity and the phase difference between the emitted p- and d-waves, respectively. These parameters are independent from any geometry-specific angles and can be found in the literature. γ is tabulated in Refs. [4, 5], while Δ can be calculated using the NIST Software *Electron Elastic-Scattering Cross-Section Database v3.2* [6].

In conclusion, the non-dipolar parameters S_{R} and S_{I} used in eq. (1) are calculated from geometry-free parameters γ and Δ, and the angles ϕ and θ mentioned above. The corresponding relations can be found in Ref. [2], eqs. 84–88, and Ref. [3], eqs. 20, 21 and 23). In Table I, we list all relevant parameters that have been used in the present study.

TABLE I. Non-dipolar parameters and relevant geometry-specific angles used for the analysis of the NIXSW data in this work. Note that the value for ϕ is an averaged value since electrons in the range from $\phi = 60°$ to $90°$ are recorded by the analyzer due to its large acceptance angle. ξ quantifies the deviation from perfect normal incidence and is defined as $\xi = 90° - \theta$.

core level	γ	Δ	S_{R}	$\lvert S_{\mathrm{I}}\rvert$	ψ	ϕ	θ	ξ
C1s	1.250	−0.18519	1.194	1.102	−0.024	75°	86.5°	3.5°
O1s	1.175	−0.25586	1.176	1.093	−0.032			

* j.felter@fz-juelich.de; m.franke@fz-juelich.de. These authors have contributed equally to this work.

[1] R. Fink, D. Gador, U. Stahl, Y. Zou, and E. Umbach, Phys. Rev. B **60**, 2818 (1999).
[2] F. C. Bocquet, G. Mercurio, M. Franke, G. van Straaten, S. Weiß, S. Soubatch, C. Kumpf, and F. S. Tautz, Comput. Phys. Commun. **235**, 502 (2019).
[3] G. van Straaten, M. Franke, F. C. Bocquet, F. S. Tautz, and C. Kumpf, J. Electron. Spectrosc. Relat. Phenom. **222**, 106 (2018).
[4] M. Trzhaskovskaya, V. Nefedov, and V. Yarzhemsky, At. Data Nucl. Data Tables **77**, 97 (2001).
[5] M. Trzhaskovskaya, V. Nefedov, and V. Yarzhemsky, At. Data Nucl. Data Tables **82**, 257 (2002).
[6] A. Jabloniski, F. Salvat, and C. J. Powell, "NIST Electron Elastic-Scattering Cross-Section Database Version 3.2" (2010).